



Engineering FeN₄ active sites onto nitrogen-rich carbon with tubular channels for enhanced oxygen reduction reaction performance

Fenghong Lu^{a,1}, Kaicai Fan^{b,1}, Lixiu Cui^a, Bin Li^b, Yu Yang^a, Lingbo Zong^{a,*}, Lei Wang^{a,c,**}

^a Key Laboratory of Eco-chemical Engineering, College of Chemistry and Molecular Engineering, Qingdao University of Science and Technology, Qingdao 266042, China

^b College of Materials Science and Engineering, Qingdao University of Science and Technology, Qingdao 266042, China

^c Shandong Engineering Research Centre of Marine Environment Corrosion and Safety Protection, College of Environment and Safety Engineering, Qingdao University of Science and Technology, Qingdao 266042, China

ARTICLE INFO

Keywords:

Single atom
Oxygen reduction reaction
Electron-withdrawing
Mass transport
Tubular channels

ABSTRACT

Nitrogen coordinated Fe single atoms (Fe-N_x SAs) anchored in carbon support is one of the most efficient electrocatalysts for oxygen reduction reaction (ORR). Engineering the microenvironment of Fe-N_x sites to achieve enhanced activity is still challenging. Herein, we theoretically demonstrate that nitrogen dopants in carbon skeletons can optimize the adsorption of ORR intermediates on Fe-N₄ sites. Then, we introduce a rational strategy to anchor Fe-N₄ sites in nitrogen-rich carbon support with abundant tubular channels (Fe-SAs@NCTCs). Fe-SAs@NCTCs exhibits encouraging ORR performance with a half-wave potential of 0.91 V in 0.1 M KOH and 0.80 V in 0.1 M HClO₄. The assembled rechargeable Zn-air battery presents high power density and operates steadily with a narrow voltage gap of 0.76 V for 650 h. The results verify that the outstanding ORR activity can be attributed to the abundant nitrogen dopant, hierarchical porous structure, and abundant tubular channels.

1. Introduction

Oxygen reduction reaction (ORR) is an imperative electrochemical reaction in those clean electrochemical energy conversion devices, including metal-air batteries and fuel cells [1–3]. Up to now, platinum group metal (PGM)-based materials are the most efficient electrocatalysts, but their prohibitive costs and global reserve scarcity seriously hamper the large-scale commercialization of the renewable energy systems [4–6]. Thus, extensive efforts have been devoted in exploring cost-effective and efficient PGM-free ORR electrocatalysts [7–9]. Amongst, 3d transition metal single atoms (TM SAs) anchored in nitrogen doped carbon support with maximized atom utilization efficiency, tunable electronic properties and fascinating catalytic properties have emerged as a new category of encouraging alternatives [10–12].

Recent studies manifest that nitrogen atoms coordinated Fe SAs (Fe-N_x moieties) are the most promising PGM-free electrocatalysts possessing excellent ORR activity [13,14]. However, there are still considerable performance disparity between Fe-N_x catalysts and the apex of the ORR volcano plot, which requires further regulations on the

microenvironment of active sites towards optimal adsorption strength of oxygenated intermediates, and enhance the kinetic activity of Fe-N_x catalysts [15,16]. Recently, tremendous research efforts have been devoted to exploring rational and feasible strategies at atomic level to facilitate the adsorption/desorption behavior of these intermediates [17–19]. For instance, coordinating both N and new heteroatoms, e.g. P and S, to Fe active sites is projected to lead charge redistributions, which lowers the binding strength of O₂ and oxygenated intermediates, and boosts the ORR activity [17,18,20,21]. Altering the environment atoms in carbon skeletons via heteroatom doping is also a promising strategy to modify the electronic structure of the Fe-N_x active sites, and enhance the kinetic activity of Fe-N_x active sites [19,22]. Despite different microenvironment of the constructed Fe-N_x catalysts, these strategies share the same idea of increasing electron transfer from Fe central atoms to the nearby atoms, which facilitates the desorption of the oxygenated intermediate [21,23]. Furthermore, the activity of electrocatalyst depends substantially on the number of accessible active sites and the mass transport ability [24–26]. Recent years have witnessed enormous endeavors to maximize accessibility of active sites since a certain fraction

* Corresponding author.

** Corresponding author at: Key Laboratory of Eco-chemical Engineering, College of Chemistry and Molecular Engineering, Qingdao University of Science and Technology, Qingdao 266042, China.

E-mail addresses: lingbozong@qust.edu.cn (L. Zong), inorchemwl@126.com (L. Wang).

¹ These authors contributed equally.

of Fe-N_x moieties are originally buried inside the nanoparticle during the preparation [27–29]. Amongst, directly anchoring the SA sites on well-graphitized carbon support with abundant micropores has been highlighted as an efficient strategy leading to high accessibility of active sites [1,30,31]. Unfortunately, the microporous nanoparticles normally possess limited local transport of protons and O₂ molecules, which required to be accelerated to fully boost the ORR activity [25,28]. To this end, it is critical to construct meso- and macropore structure with optimal mass transport channels to adequately convey the reactants and electrolytes into the active sites [32,33]. Hence, an ideal electrocatalyst is expected to possess abundant active sites with excellent intrinsic activity, maximized accessibility of active sites and optimal mass transport channels.

Here, enlightened by the theoretical predication, which revealed the pivotal role of nitrogen dopant in carbon skeletons in serving an electron-withdrawing environment and boosting ORR activity of Fe-N₄ sites, we report a facile synthesis of Fe SAs anchored in the nitrogen-rich carbon support with abundant tubular channels (Fe-SAs@NCTCs). Anchoring the intrinsically active Fe SAs in carbon support offers maximized Fe-N₄ active sites with electrochemical accessibility, and the hierarchical porous structure with tubular channels affords outstanding rapid mass transport during ORR process. Consequently, Fe-SAs@NCTCs exhibits remarkable ORR performances with high half-wave potential ($E_{1/2}$) of 0.91 V (vs. RHE) in 0.1 M KOH and $E_{1/2}$ of 0.80 V (vs. RHE) in 0.1 M HClO₄. The fabricated rechargeable Zn–air battery displays promising performance, including large power density and high specific capacity, outperforming the Pt/C + RuO₂-based battery. Specifically, the Fe-SAs@NCTCs-based Zn–air battery can operate steadily for 650 h with a narrow discharge/charge gap of 0.76 V. This work exemplifies an efficient SA-based electrocatalyst for ORR, and projects a rational strategy, which involves controlling the atomic configuration of active sites and optimizing the morphology of electrocatalyst, to boost the ORR activity of SAs.

2. Experimental section

2.1. Synthesis of carbon with tubular channels (CTCs)

Nanofiber precursor was firstly fabricated according to our recently developed approach with a minor modification. Typically, 0.36 g glucose and 0.42 g NaNO₃ were dissolved in 6 mL deionized water. 0.50 g melamine was then added in and stirred for 10 min. After the addition of hydrochloric acid (1 M, 3 mL), the solution turned into a gel. The nanofiber precursor was collected after freeze-drying.

CTCs was prepared via a two-step pyrolysis process. The nanofiber precursor was firstly annealed in N₂ atmosphere at 280 °C for 6 h to accomplish the pre-carbonization. The obtained powder was then freeze-dried after being washed with deionized water to remove the retained salt, and heated under the protection of N₂ atmosphere at 900 °C for 2 h. Finally, CTCs was obtained and collected.

2.2. Synthesis of Fe-SAs@NCTCs

CTCs was firstly dispersed in the solution containing 0.125 M FeCl₃ solution, and the mixture was stirred continuously for 24 h. The product with the effectively adsorbed Fe³⁺ was then collected, washed with deionized water, and dried. Afterward, the collected samples were dispersed in 10 mL deionized water and 10 mL ammonium hydroxide solution, and the solution was then transferred to an autoclave and heated at 150 °C for 12 h. The obtained precipitant (denoted as Fe, N@CTCs) was collected by centrifugation and washed with water and ethanol. Finally, the dried precipitant was thermal activated at 900 °C for 2 h in N₂ atmosphere, and the product was labeled as Fe-SAs@NCTCs.

2.3. Synthesis of NCTCs and Cu-SAs@NCTCs

NCTCs were prepared following the similar procedures as Fe-SAs@NCTCs except without adding FeCl₃. Cu-SAs@NCTCs were prepared by the same approach as Fe-SAs@NCTCs except replacing the FeCl₃ with CuCl₂.

2.4. Synthesis of Fe-SAs@CTCs and Fe-SAs@NCs

Fe-SAs@CTCs was prepared using CTCs through similar procedures as fabricating Fe-SAs@NCTCs, except that the ammonia hydroxide solution was not added during the hydrothermal treatment. Fe-SAs@NCs without tubular channels was also prepared by directly annealing the precursors of glucose, melamine, and FeCl₃·6 H₂O at 900 °C in N₂.

2.5. Characterizations

X-ray power diffraction (XRD) patterns were collected on a Rigaku-D_{max} 2500 diffractometer. X-ray photoelectron spectroscopy (XPS) date and Raman spectra were collected on ESCALAB 250Xi X-ray photoelectron spectrometer (Thermo Scientific) and on LabRAM HR800, respectively. The N₂ adsorption/desorption isotherms were acquired on ASAP 2020 physisorption analyzer. Morphology of electrocatalysts were observed on scanning electron microscope (SEM, Sigma 500, Zeiss), transmission electron microscopy (TEM, JEM-2100 F), and spherical aberration-corrected scanning transmission electron microscopy (STEM, Titan Cubed Themis G2 60–300). Inductively coupled plasma mass spectrometry (ICP-MS, Thermo iCAP RQ) was employed to determine the metal contents in the electrocatalysts. X-ray absorption fine structure (XAFS) date were collected at the Beijing Synchrotron Radiation Facility (1W1B), and the obtained data were processed using the ATHENA and Artemis from IFEFFIT suite.

2.6. Electrochemical characterizations

CHI 760E electrochemical workstation and rotational equipment with a typical three electrode system were used for all electrochemical tests. Graphite rod and KCl-saturated Ag/AgCl electrode were exploited as counter and reference electrode, respectively. The electrocatalyst inks were prepared by dispersing 5 mg electrocatalysts with a mixed solution containing 20 μL 5% Nafion 117 solution, 240 μL water and 740 μL isopropanol. Then, the working electrode was prepared by pasting 10 μL of the electrocatalyst onto the rotating disk electrode (RDE, d = 5.0 mm) or rotating ring-disk electrode (RRDE, d = 5.61 mm) with the loading capacity of 0.255 mg cm^{−2}.

ORR tests were implemented in O₂-saturated 0.1 M KOH solution or 0.1 M HClO₄. All potentials were calibrated to the reversible hydrogen electrode (RHE) via the equation: E (vs. RHE) = E (Ag/AgCl) + 0.059·pH + 0.1976 − 0.95 iR. Linear sweep voltammetry (LSV) polarization curves were recorded at the scan rate of 5 mV s^{−1}. Long-term durability of the prepared electrocatalysts and Pt/C benchmark was evaluated by performing chronoamperometry at 0.8 V, and comparing LSV curves before and after thousands of cyclic voltammetry (CV) cycles.

The electron transfer number (n) were calculated based on the Koutecký-Levich equations:

$$\frac{1}{j} = \frac{1}{j_l} + \frac{1}{j_k} = \frac{1}{B\omega^{1/2}} + \frac{1}{j_k}$$

$$B = 0.62nFC_0D^{2/3}\nu^{-1/6}$$

j , j_l , and j_k are the measured, diffusion-limiting, and kinetic current density, respectively. ω represents the electrode's angular velocity (rad s^{−1}). F is the Faraday constant (96485 C mol^{−1}). C_0 and D is the saturated O₂ concentration (1.21 × 10^{−6} mol cm^{−3}) and the diffusion

coefficient of O₂ in 0.1 M KOH ($1.9 \times 10^{-5} \text{ cm}^2 \text{ s}^{-1}$), respectively. ν is the kinetic viscosity ($0.01 \text{ cm}^2 \text{ s}^{-1}$). RRDE measurements were performed with the ring electrode potential of 1.2 V. n and H₂O₂ yield (H₂O₂%) of ORR were determined according to the following equations:

$$n = \frac{4j_d}{j_d + j_r/N}$$

$$\text{H}_2\text{O}_2\% = 200 \frac{j_r/N}{j_d + j_r/N}$$

where N , j_d and j_r are the current collection efficiency of the Pt ring electrode (0.37), the disk current and the ring current, respectively.

OER performance was measured in 1 M KOH electrolyte in three electrode system, in which RDE glassy carbon electrode with electrocatalyst, Hg/HgO and graphite rod were used as working, reference and counter electrode, respectively. The faradaic efficiency (FE) of OER was assessed on RRDE electrode. Specifically, a fixed current of 300 μA was applied on the glassy carbon disk electrode to yield O₂, and the ring current was recorded when a constant potential of 0.4 V (vs. RHE) was employed on the Pt ring electrode to reduce the O₂ generated from the disk electrode. Thus, FE was calculated via the following equation:

$$\text{FE} = \frac{j_r}{N \times j_d}$$

2.7. Zn-air battery tests

The home-made Zn-air battery was assembled using carbon paper coated with electrocatalyst (loading: 1 mg cm^{-2}) as air cathode, Zn plate as anode and 6 M KOH containing 0.2 M Zn(Ac)₂ aqueous solution as electrolyte.

2.8. Computational method

The density functional theory (DFT) calculations with the consideration of spin-polarization were carried out by the Vienna ab initio Simulation Package (VASP) [34]. The generalized gradient approximation (GGA) with Perdew Burke Ernzerhof (PBE) functional was applied to process the exchange-correlation part. The projected augmented plane wave (PAW) was used to describe the core-state of all elements. To avoid the artificial interaction between the slabs, the van der Waals correction was added into the model using the Grimme methods (DFT+D3) [35]. The cut-off energy was chosen to be 500 eV; the positions of all atoms were relaxed until the average force per atom decrease to 0.01 eV \AA^{-1} ; the Brillouin zone integration is carried out selecting a k-point mesh of $2 \times 2 \times 1$ in the structure optimization, while $4 \times 4 \times 1$ in the calculation of density of state. All intermediates free energies were calculated based on the zero-point energy (ZPE) corrections and thermodynamics corrections (entropy correction) to the calculated DFT energies as following formulas:

$$G_{\text{ads}}^{\text{surf}} = H_{\text{ads}}^{\text{surf}} - TS = E_{\text{ads}}^{\text{surf,DFT}} + \Delta\text{ZPE}_{\text{ads}}^{\text{surf}} - TS$$

$$G_{\text{ads}} = H_{\text{ads}} - TS = U_{\text{ads}} + pV - TS = E_{\text{ads}} + \Delta\text{ZPE} + pV - TS$$

The d-band centers of surface sites were calculated by the following formula:

$$\varepsilon_d = \frac{\int \varepsilon \text{DOS}(\varepsilon) d\varepsilon}{\int \text{DOS}(\varepsilon) d\varepsilon}$$

3. Results and discussions

3.1. DFT calculations

The density functional theory (DFT) calculations were firstly conducted to explore the crucial role of the nitrogen dopant in carbon

skeletons on tuning ORR activity of atomically-dispersed Fe-N₄ sites. The configuration of Fe-(N-C₂)₄-2N was constructed by substituting two nearest carbon atoms of Fe-(N-C₂)₄ sites with nitrogen atoms, as shown in Fig. 1a. The charge density distribution was firstly examined (Fig. 1b; Table S1 and S2). For both configurations, electrons are observed transferring from Fe to the nearby N atoms and the originally electro-neutral Fe atoms become positively charged [19,36–38]. Notably, Fe atom in Fe-(N-C₂)₄-2N is more positively charged than Fe-(N-C₂)₄, confirming the strong electron-withdrawing effect of nitrogen dopant on the Fe-(N-C₂)₄ sites, and the regulated electronic structure is proposed to alter the adsorption strength of oxygenated intermediates [22,39,40]. DFT calculated density of states (DOS) and d-band center (ε_d) were then calculated to reveal the electronic structure property of the central Fe atom. As displayed in Fig. 1c, the ε_d of Fe-(N-C₂)₄-2N is -1.51 eV , which is lower than that of Fe-(N-C₂)₄ (-1.33 eV), the down-shifted d-band center induces weakened binding strength of oxygenated intermediates on Fe-(N-C₂)₄-2N configuration [19,40]. It has been intensively demonstrated that the rate-determining step on Fe-N₄ sites is the last OH* desorption step, herein, the weakened interaction between them is imperative to achieve enhanced ORR activity [41]. The adsorption-desorption behaviors of ORR intermediates were then systematically explored. The DFT-optimized intermediates adsorption configurations of Fe-(N-C₂)₄ and Fe-(N-C₂)₄-2N sites are presented in Fig. 1d and Fig. S1. The calculated intermediates adsorption free energies (ΔG_{OOH^*} , ΔG_{O^*} and ΔG_{OH^*}) under the equilibrium potential (U) of 0 V (Fig. 1e and Table S3) indicate ΔG_{OH^*} of Fe-(N-C₂)₄-2N (0.47 eV) are obviously larger than that of Fe-(N-C₂)₄ (0.28 eV), illustrating OH* is more favorable to be desorbed from Fe-(N-C₂)₄-2N than Fe-(N-C₂)₄ [36, 42]. At $U = 1.23 \text{ V}$, the last step of desorption of OH* is the most endothermic step for both configurations, supporting the strong adsorption of OH* on both configurations (Fig. S2 and Table S4). Whereas, Fe-(N-C₂)₄-2N possesses a lower energy barrier of 0.75 eV than Fe-(N-C₂)₄ (0.95 eV), implying the enhanced intrinsic catalytic activity of Fe-(N-C₂)₄-2N and the superiority of the nitrogen dopant in carbon skeletons for boosted ORR [11,38].

3.2. Synthesis and structural characteristics of Fe-SAs@NCTCs

Inspired by the theoretical calculations, single-atom Fe-N₄ catalysts with abundant nitrogen dopant (Fe-SAs@NCTCs) were prepared and the tubular channels were constructed to maximize the accessibility of active sites and minimize the kinetic barrier on mass transport. The fabrication of Fe-SAs@NCTCs is schematically illustrated in Fig. 2a. Firstly, the xerogels assembled by compacted nanofibers (Fig. S3) were prepared via the reported method with a minor modification [43]. After the controlled carbonization of the xerogels at a low temperature of 280 °C, carbon support with well-defined tubular channels (CTCs) were obtained (Fig. S4 and S5). Afterward, Fe³⁺ ions and supplemented N resources were introduced into CTCs, and thermal activation was subsequently conducted at 900 °C under N₂ atmosphere to obtain Fe-SAs@NCTCs. The Fe-free nitrogen-doped carbon with tubular channels (NCTCs) and Fe-SAs@CTCs with low nitrogen content were also prepared as comparison.

The morphology of Fe-SAs@NCTCs was evaluated using the scanning electron microscopy (SEM) and transmission electron microscopy (TEM). SEM images (Figs. 2b and 2c) reveal the honeycomb-like structure of Fe-SAs@NCTCs with the presence of abundant pores. Moreover, low-tortuosity tubular channels are observed (Fig. 2d), which are supposed to be transformed from the compacted nanofibers [44,45]. TEM image in Fig. 2e presents a striking contrast between the hollow core portion and carbon walls, further supporting the formation of well-defined tubular channels throughout the carbon support [15, 46–48]. Notably, these tubular channels are randomly stick in the carbon support, which could efficiently render the three-dimensional (3D) mass transport pathways during electrochemical reaction [49,50]. The TEM image in Fig. 2f distinctly addresses the low-tortuosity tubular

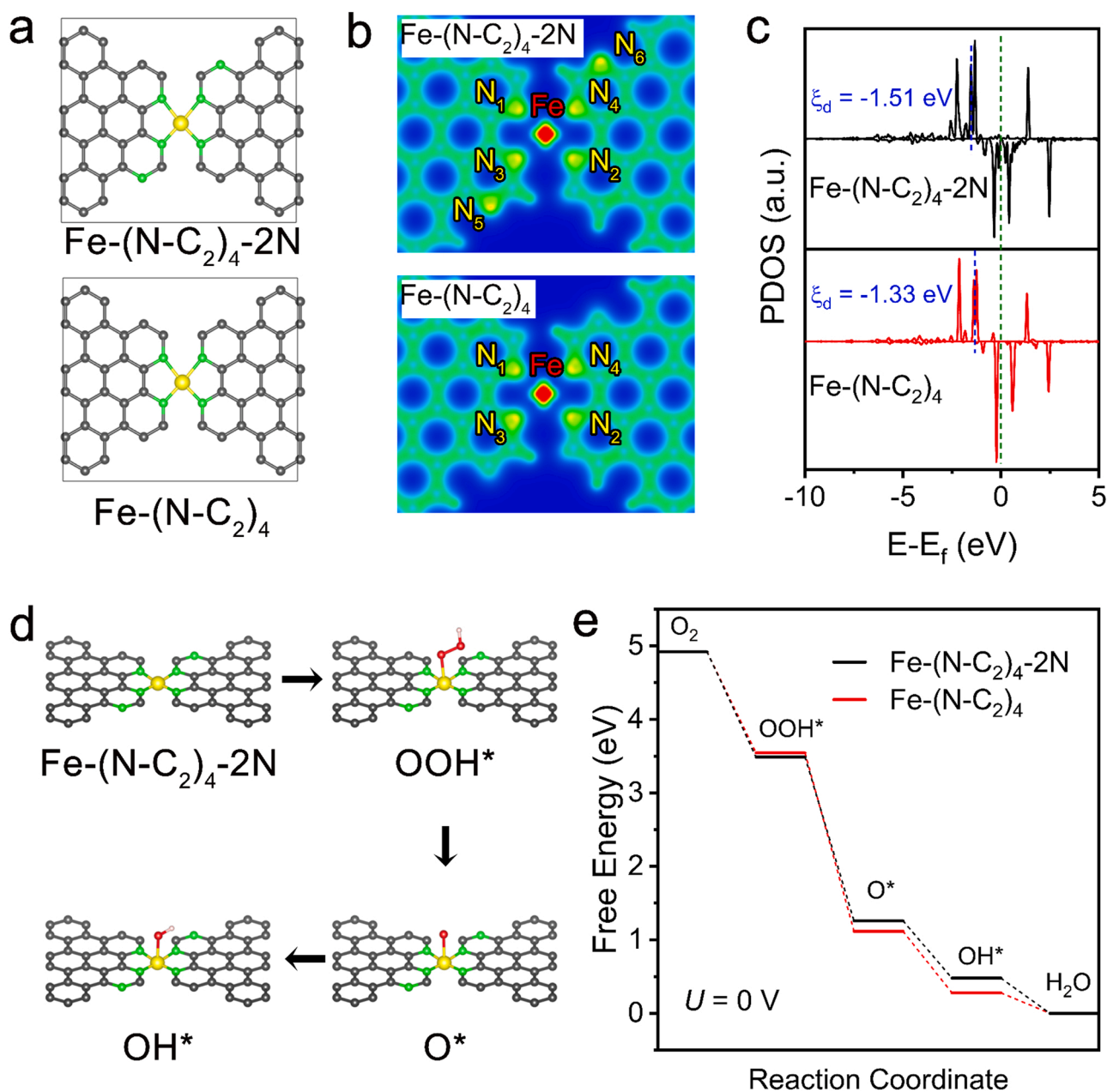


Fig. 1. (a) TOP view of DFT optimized Fe-(N-C₂)₄ and Fe-(N-C₂)₄-2N. (b) Charge density distribution of Fe-(N-C₂)₄-2N and Fe-(N-C₂)₄. (c) Projected density of states (PDOS) of Fe atoms in Fe-(N-C₂)₄-2N and Fe-(N-C₂)₄. (d) DFT-optimized adsorption configurations of intermediates on Fe-(N-C₂)₄-2N. (e) Calculated Gibbs free energy diagrams for ORR on the Fe-(N-C₂)₄ and Fe-(N-C₂)₄-2N (U = 0 V).

channels with the carbon walls and no Fe-derived nanoparticles exist in the carbon walls. Additionally, SEM and TEM images of NCTCs and Fe-SAs@CTCs in Fig. S6 and S7 reveal their morphological structures closely resembled to Fe-SAs@NCTCs, evidencing the adsorbed Fe atoms or supplemented N resources is not crucial in determining the morphology of the electrocatalysts. Particularly, the introduced approach can be extended to prepare other SA-based electrocatalyst with identical morphology as revealed in Fig. S8.

The pore structure characteristics of Fe-SAs@NCTCs were further evaluated by N₂ adsorption/desorption measurements. As shown by the isotherms (Fig. 2g), it displays a type H₄ hysteresis loop with a composite of Type I and II adsorption isotherm, demonstrating the coexistence of micropores, mesopores and macropores [51]. In addition, both BJH and DFT model were applied to identify the pore-size distribution in the ranges from micropores to mesopores. As shown in the inset of Fig. 2g and Table S5, there are plentiful micropores and mesopores with

size distribution centered around 0.7 nm and 3.9 nm in Fe-SAs@NCTCs, which intensively demonstrate that the enriched hierarchical pores exist on the carbon walls. Thus, Fe-SAs@NCTCs possesses a high Brunauer-Emmett-Teller (BET) surface area of 503 m² g⁻¹ with the micropore volume of 0.20 cm³ g⁻¹ and mesopore volume of 0.09 cm³ g⁻¹. The above analysis results confirm the unique trimodal-porous structure of Fe-SAs@NCTCs. Specifically, the unique morphological structure with low-tortuosity tubular channels and interconnected hierarchical pores on the carbon walls could significantly maximize the exposure of active sites and facilitate the mass transport during the electrochemical reactions [52,53].

The structural and compositional features of Fe-SAs@NCTCs were further studied at the element and atomic level. The high-resolution TEM (HR-TEM) image in Fig. 3a displays the disordered carbon structures, which has randomly oriented graphitic domains. Obviously, no metal-containing nanoparticles or clusters can be observed in Fe-

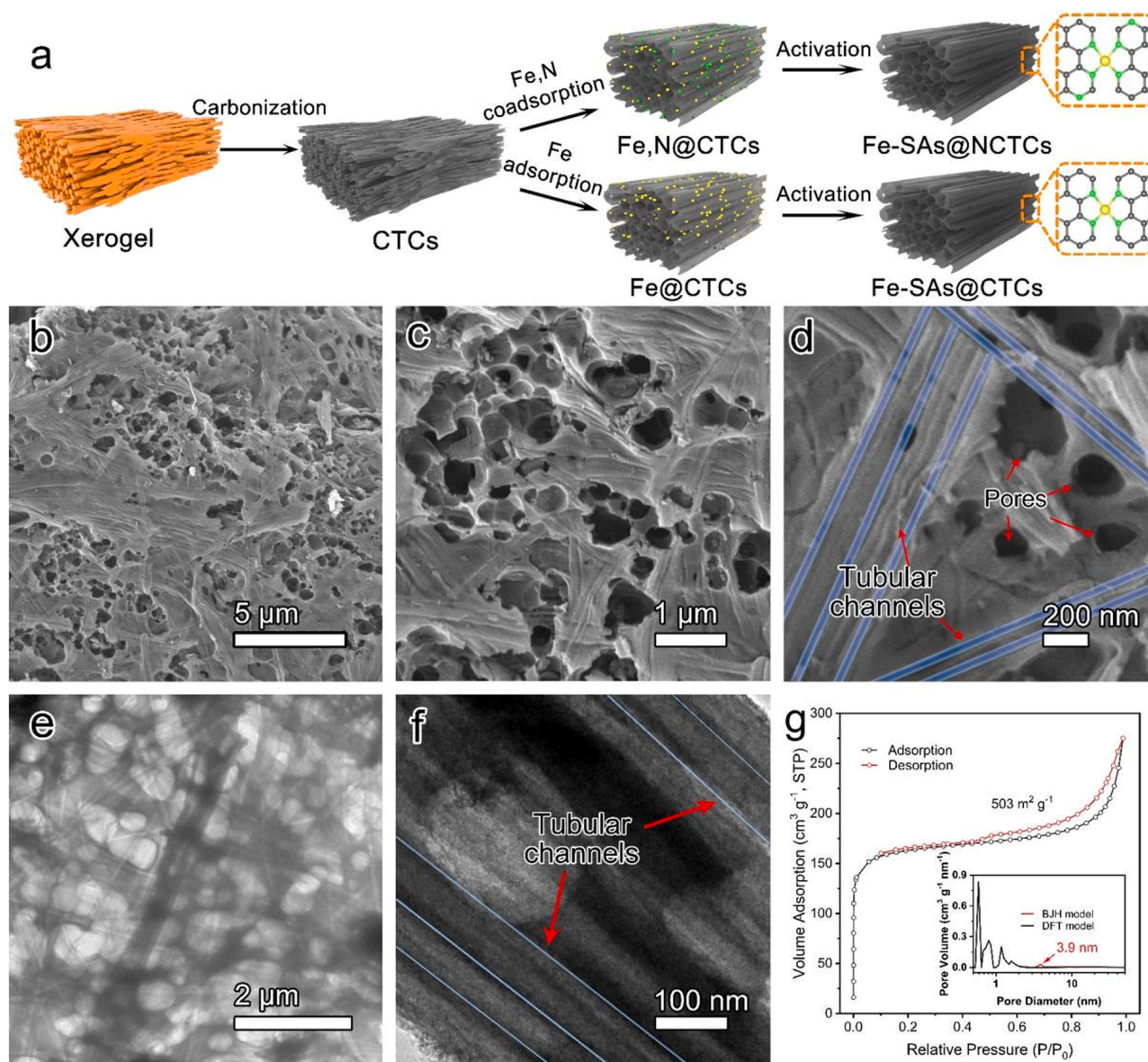


Fig. 2. (a) Schematic illustration of the synthetic process of various electrocatalysts. b, c, d) SEM images and e, f) TEM images of Fe-SAs@NCTCs. g) N₂ adsorption-desorption isotherms for Fe-SAs@NCTCs with the inset showing the corresponding pore-size distribution curve.

SAs@NCTCs. Furthermore, the corresponding energy-dispersive X-ray (EDX) mappings in Fig. 3b reveal the homogeneous distribution of Fe, N, and C elements, and support the presence of the atomically dispersed Fe species. The aberration-corrected high-angle annular dark-field scanning transmission electron microscopy (AC HAADF-STEM) images (Fig. 3c and Fig. S9) show that high-density of individual bright spots assigning to Fe SAs are homogeneously distributed in Fe-SAs@NCTCs. The Fe content of Fe-SAs@NCTCs was determined to be 1.7 wt %, which was similar to that of Fe-SAs@CTCs (1.9 wt %), by inductively coupled plasma mass spectrometry (ICP-MS).

The XRD pattern of Fe-SAs@NCTCs, which is analogous to NCTCs, exhibits two broad diffraction peaks at $\sim 24^\circ$ and 44° , ascribing to (002) and (101) lattice planes of graphitic carbon (Fig. S10) [54]. There are no other distinguished XRD peaks, excluding the presence of Fe-based compound. The Raman spectroscopy was employed to further evaluate the molecular morphology of the as developed electrocatalysts. As shown in Fig. S11, the intensity ratio between D-band to G-band (I_D/I_G) for Fe-SAs@NCTCs (1.11) is similar to that of NCTCs (1.09), which demonstrates that the carbon structure with relatively high disorder is

retained even when Fe atoms were doped into the carbon matrix. The elemental information of Fe-SAs@NCTCs, Fe-SAs@CTCs and NCTCs were then characterized and compared using X-ray photoelectron spectroscopy (XPS). The XPS survey spectra (Fig. S12 and Table S6) depict the existence of C and N in these electrocatalysts. Meanwhile, the N content of Fe-SAs@NCTCs reaches a high level of 3.1%, which is same as NCTCs (3.1%) and 1.47 times as much as Fe-SAs@CTCs (2.1%). This result illustrates the efficiency in elevating the doping level of nitrogen atoms through the ammonia assisted hydrothermal process. Besides, there are no obvious Fe signals for Fe-SAs@NCTCs and Fe-SAs@CTCs, which supports the low content of Fe species. Moreover, as revealed by the high-resolution Fe 2p spectra of both samples in Fig. S13a and Fig. S14a, the deconvoluted peaks centered at 709.5 and 722.7 eV correspond to the Fe 2p_{3/2} and Fe 2p_{1/2}, respectively, revealing the oxidation state of Fe is around +2 and excluding the formation of Fe-derived nanoparticles [55]. The high-resolution N 1s spectra of Fe-SAs@NCTCs and Fe-SAs@CTCs was fitted into five peaks (Fig. S13b and S14b), which could be ascribed to pyridinic N (398.3 eV), Fe-N_x (399.6 eV), pyrrolic N (400.9 eV), graphitic N (401.7 eV), and oxidized

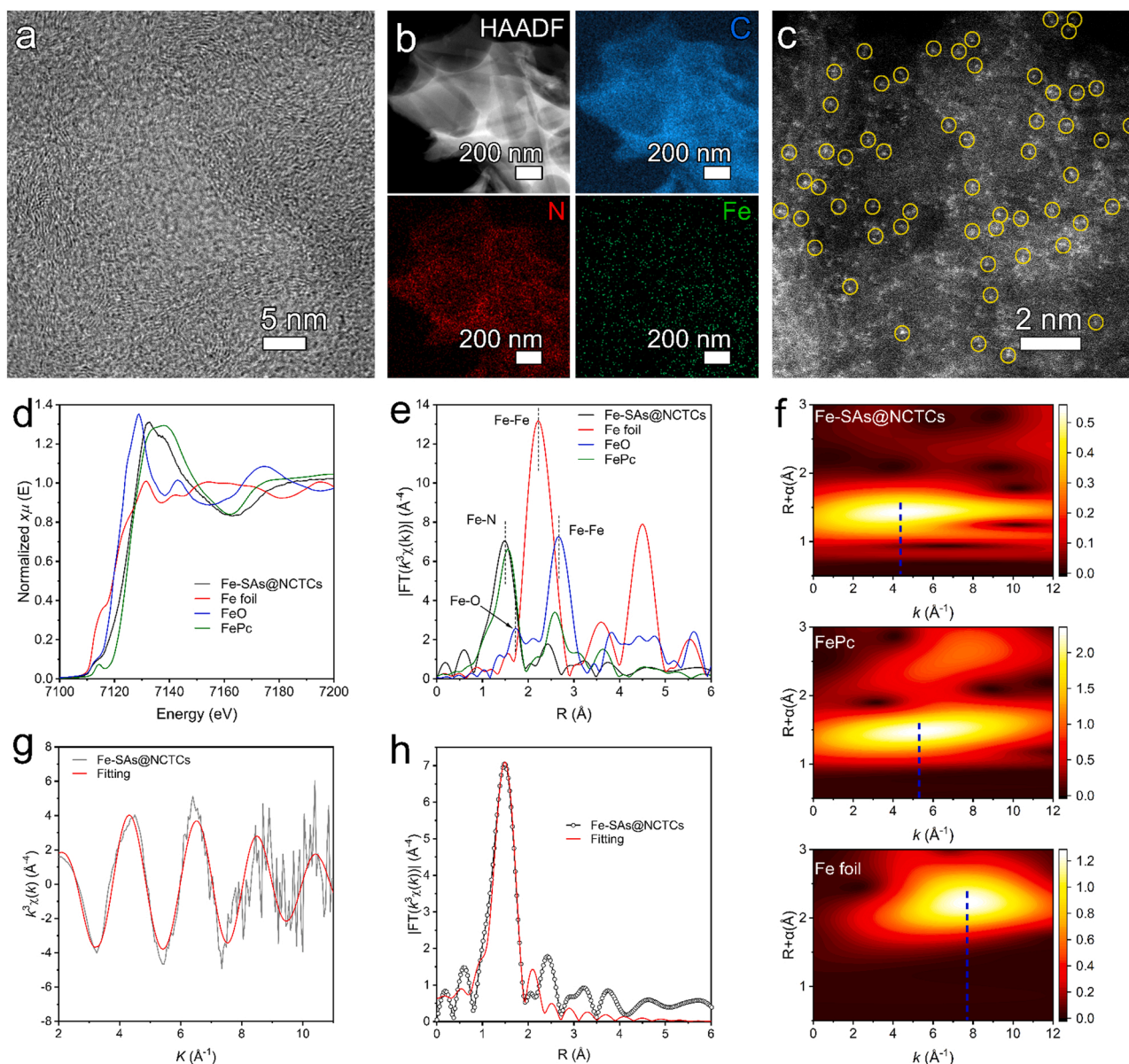


Fig. 3. (a) HR-TEM, (b) EDX element mapping images, and (c) AC-HAADF-STEM image of Fe-SAs@NCTCs. (d) XANES spectra of Fe K-edge, (e) Fourier transforms of EXAFS spectra of Fe-SAs@NCTCs, Fe foil, FeO and FePc at Fe K-edge. (f) WT-EXAFS plots of Fe-SAs@NCTCs, FePc and Fe foil, respectively. (g, h) First shell (Fe-N) fitting of FT-EXAFS spectra for Fe-SAs@NCTCs at k and R space, respectively.

N (403.2 eV). Specifically, the atomic ratio of graphitic N in Fe-SAs@NCTCs is noticeably higher than that in Fe-SAs@CTCs (Table S7). The above analysis results support the generation of atomically dispersed Fe-N_x moieties for both samples [56], and Fe-SAs@NCTCs possesses more successfully doped N atoms in carbon skeleton.

The local coordination environment of Fe in Fe-SAs@NCTCs were then systematically investigated by the synchrotron-based X-ray absorption near-edge structure (XANES) and extended X-ray absorption fine structure (EXAFS). Fig. 3d exhibits the Fe K-edge XANES spectra of Fe-SAs@NCTCs and the reference samples. The absorption edge position for Fe-SAs@NCTCs is near to FeO and FePc, implying that the oxidation state of Fe is about 2+. The detailed structural information was obtained by EXAFS. As displayed by the Fourier-transformed k^3 -weighted EXAFS (FT-EXAFS) spectrum in Fig. 3e, Fe foil, FeO and FePc exhibit Fe-Fe, Fe-O and Fe-N paths at 2.20 Å, 1.60 Å and 1.50 Å, respectively. Notably, Fe-SAs@NCTCs possess a prominent peak centered at 1.5 Å, which is almost identical to FePc, evidencing the presence of the first

shell Fe-N scattering path [3,53]. No Fe-Fe species can be observed, further confirming that no Fe-derived nanoparticles existing in Fe-SAs@NCTCs [57,58]. To distinguish the backscattering atoms in k space, the wavelet transform (WT)-EXAFS was conducted. The WT-EXAFS of Fe-SAs@NCTCs in Fig. 3f exhibits only one contour intensity maximum at 4.0 Å⁻¹ in k space, which can be ascribed to the Fe-N first shell coordination [38,59]. The above results further disclose that Fe is primarily present as SAs instead of Fe-derived crystalline structures in Fe-SAs@NCTCs. To identify the coordination configuration of central Fe atoms in Fe-SAs@NCTCs, EXAFS fitting was conducted. The EXAFS fitting curve in Figs. 3g and 3h and the extracted structural parameters in Table S8, demonstrate that the central Fe atoms have an average coordination number of 4.4 with the Fe-N bonding distance of 1.97 Å in the first shell. These results reveal that the Fe atoms in Fe-SAs@NCTCs are predominantly coordinated with four N atoms yielding Fe-N₄ configuration [26]. The coordination configuration of atomically dispersed Fe atoms in Fe-SAs@CTCs (Fig. S15) was also identified by XAS measurements, which possessed analogous Fe-N₄

configuration to Fe-SAs@NCTCs (Fig. S16 and Table S8). It should be noted that the Fe-K pre-edge features, relating to $1s \rightarrow 3d$ metal electronic transitions, reveal that both samples possess a main peak centered at 7112.8 eV, and demonstrate the identical oxidation state of Fe (Fig. S17) [60,61]. In addition, the Fe-K pre-edge of both samples can be deconvoluted into two peaks assignable to Fe^{2+} and Fe^{3+} , and Fe-SAs@NCTCs presents a higher content of Fe^{3+} than Fe-SAs@CTCs. Therefore, N dopants in the carbon skeleton increase the electron transfer from the Fe atoms to the carbon support, decrease the electron density of Fe, and are expected to optimize the adsorption of oxygen intermediates.

3.3. Electrocatalytic ORR performance of Fe-SAs@NCTCs

The ORR activities of Fe-SAs@NCTCs, Fe-SAs@CTCs and NCTCs were evaluated and compared with commercial Pt/C in both O_2 -saturated alkaline (0.1 M KOH) and acid (0.1 M HClO_4) electrolyte. Linear sweep voltammetry (LSV) polarization curves obtained in 0.1 M KOH (Fig. 4a) reveal that Fe-SAs@NCTCs possess better ORR activity in terms of higher onset potential ($E_{\text{onset}} = 1.02$ V) and half-wave potential ($E_{1/2} = 0.91$ V) than NCTCs ($E_{\text{onset}} = 0.99$ V, $E_{1/2} = 0.86$ V), demonstrating the essential role of Fe SAs as active sites in enhancing the ORR activity.

The critical role of the increased doping level of N atoms in boosting the ORR activity was also identified by the inferior ORR activity of Fe-SAs@CTCs ($E_{\text{onset}} = 0.94$ V, $E_{1/2} = 0.82$ V). Specifically, Fe-SAs@NCTCs exhibits superior catalytic activity than Pt/C benchmark ($E_{\text{onset}} = 0.99$ V, $E_{1/2} = 0.88$ V) and most recently reported single-atom electrocatalysts (Table S9). In addition, the ORR limiting current density of Fe-SAs@NCTCs reaches a high value of 5.4 mA cm^{-2} , which is larger than that for Pt/C (5.1 mA cm^{-2}), reflecting the excellent mass transfer ability of the highly porous carbon structure with tubular channels. Moreover, the kinetic current density (j_k) of Fe-SAs@NCTCs exceeds those of Fe-SAs@CTCs, NCTCs and Pt/C at the potential of 0.85 V (Fig. S18), demonstrating much faster reaction kinetics, and again evidencing the exceptionally good ORR activity. The accelerated reaction kinetic of Fe-SAs@NCTCs is further supported by the smallest Tafel plot slope (51 mV dec^{-1}) among all these electrocatalysts as shown in Fig. 4b [15,62]. These results demonstrate that the Fe-SAs@NCTCs displays remarkable ORR performance, surpassing the Pt/C benchmark. The significantly higher ORR activity of Fe-SAs@NCTCs than Fe-SAs@CTCs and NCTCs evidences the synergistic effect between the nitrogen-rich carbon support and Fe- N_4 moieties in accelerating the ORR reaction process.

Besides, the calculated electron transfer number (n) of Fe-

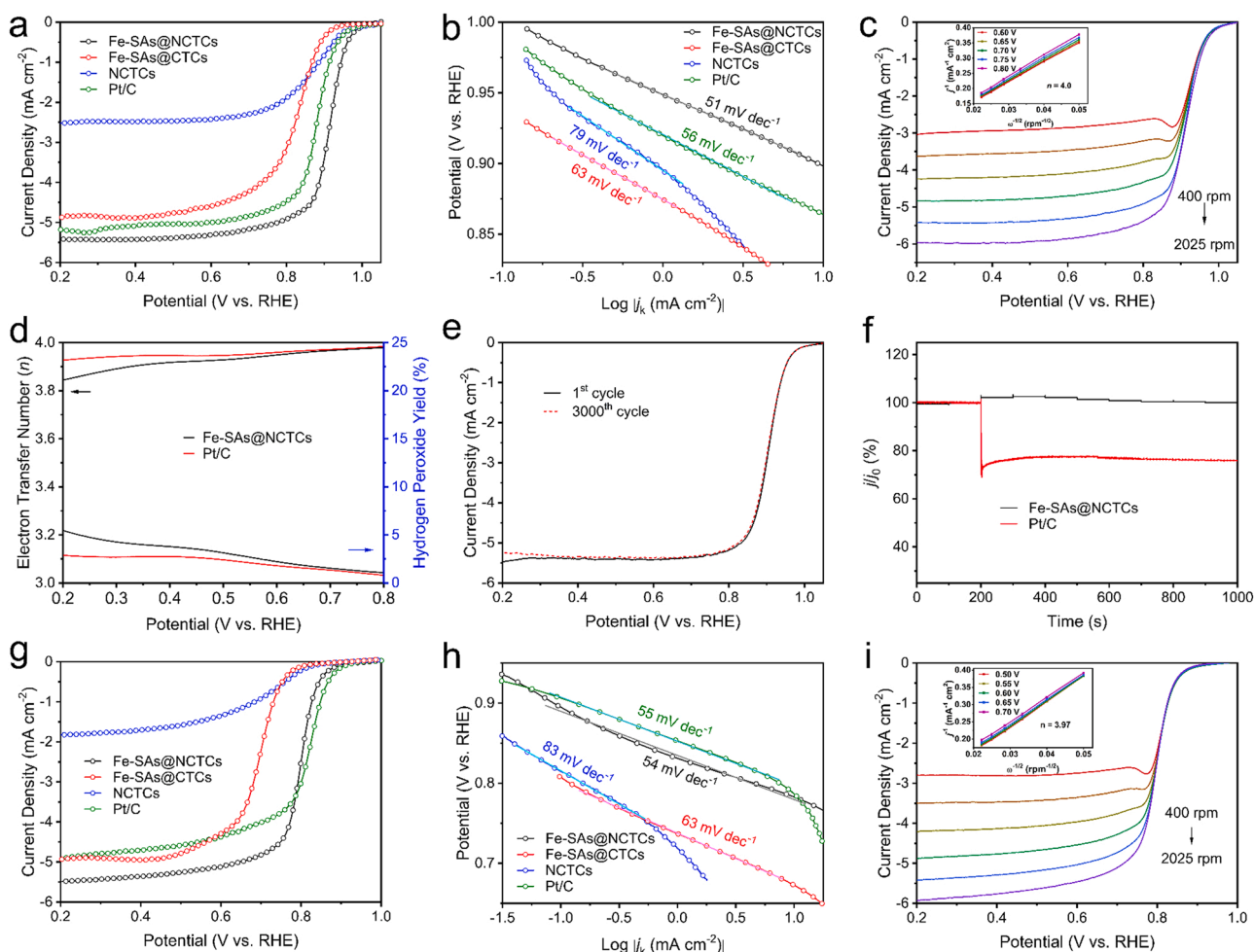


Fig. 4. (a) LSV polarization curves, and b) Tafel plots of Fe-SAs@NCTCs, Fe-SAs@CTCs, NCTCs and Pt/C measured at 1600 rpm in O_2 -saturated 0.1 M KOH. c) LSV curves of Fe-SAs@NCTCs recorded at different rotation speeds recorded in O_2 -saturated 0.1 M KOH. Inset: the corresponding K-L plots obtained from the respective LSV curves. d) Electron transfer number n (top) and H_2O_2 yield (bottom) vs. potential for Fe-SAs@NCTCs and Pt/C derived from the RRDE tests. e) 1st and 3000th ORR polarization curves of Fe-SAs@NCTCs obtained in O_2 -saturated 0.1 M KOH. f) Chronoamperometric responses of Fe-SAs@NCTCs and Pt/C before and after the injection of 10 mL methanol into 70 mL 0.1 M KOH electrolyte at 0.8 V (vs. RHE). g) LSV polarization curves, and h) Tafel plots of Fe-SAs@NCTCs, Fe-SAs@CTCs, NCTCs and Pt/C measured at 1600 rpm in O_2 -saturated 0.1 M HClO_4 . i) LSV curves of Fe-SAs@NCTCs recorded at different rotation speeds recorded in O_2 -saturated 0.1 M HClO_4 . Inset: the corresponding K-L plots obtained from the respective LSV curves.

SAs@NCTCs based on Koutecky-Levich (K-L) plots is 4.0 (Fig. 4c), signifying an efficient four-electron transfer process [63]. Besides, the ORR reaction pathway of Fe-SAs@NCTCs is also confirmed by rotating ring-disk electrode (RRDE) measurements (Fig. 4d and Fig. S19). Notably, H_2O_2 yield maintains below 5% and n is calculated to be around 4 over the potential range from 0.2 to 0.8 V, which is consistent with the results calculated from the K-L equations, supporting ORR on Fe-SAs@NCTCs proceeds via four-electron transfer pathway [64]. The accessible active site density (SD) of Fe-SAs@NCTCs was quantified by conducting the in situ electrochemical reduction of NO in aqueous nitrite solution (Fig. S20) [65]. As calculated from the reductive stripping charge CV, Fe-SAs@NCTCs achieved a remarkable SD of 7.8×10^{19} sites per gram, which demonstrates the existence of plentiful accessible Fe-N₄ sites for ORR. In addition, electrocatalysts, denoted as Fe-SAs@NCs, without porous structure and tubular channels were prepared by directly annealing the precursors of glucose, melamine, and $\text{FeCl}_3 \cdot 6\text{H}_2\text{O}$ in N_2 . As demonstrated in Fig. S21, Fe-SAs@NCs shows much inferior ORR activity compared to Fe-SAs@NCTCs. Therefore, the remarkable ORR activity of Fe-SAs@NCTCs can be attributed to the boosted intrinsic activity, high SD and facilitated mass transport structure, which were realized by the introduced material preparation strategy.

ORR stability of Fe-SAs@NCTCs was further evaluated by the accelerated degradation test (ADT). As shown in Fig. 4e, $E_{1/2}$ experienced a negligible decrease after 3000 continuous cycles. The chronoamperometry test was also applied to assess the durability of Fe-SAs@NCTCs (Fig. S22), which revealed an extremely high durability with only $\sim 7\%$ current loss after continually running for 40,000 s. The robustness of Fe-SAs@NCTCs was evaluated by characterizing the one after long-term stability test. SEM, TEM and STEM images visually attest that the morphology of Fe-SAs@NCTCs and single Fe atoms was well maintained after long-term stability test (Fig. S23 – S25). In addition, superior immunity to methanol is observed for Fe-SAs@NCTCs. As displayed in Fig. 4f, after the introduction of methanol into the electrolyte, the current density of Pt/C declined sharply, while no obvious change was observed for Fe-SAs@NCTCs. The excellent methanol tolerance property guarantees the potential application of Fe-SAs@NCTCs in direct methanol fuel cells.

In addition to the remarkable ORR performance in alkaline solution, Fe-SAs@NCTCs exhibits excellent performance in acid solution. As shown by the LSV curves in Fig. 4g, the onset and half-wave potentials for Fe-SAs@NCTCs ($E_{\text{onset}} = 0.90$ V, $E_{1/2} = 0.80$ V) is much higher than Fe-SAs@CTCs ($E_{\text{onset}} = 0.81$ V, $E_{1/2} = 0.70$ V) and NCTCs ($E_{\text{onset}} = 0.81$ V, $E_{1/2} = 0.72$ V), and comparable to those of Pt/C benchmark ($E_{\text{onset}} = 0.91$ V, $E_{1/2} = 0.83$ V). It should be noted that the ORR performance of Fe-SAs@NCTCs surpasses most of the recently reported electrocatalysts as shown in Table S10. Remarkably, Fe-SAs@NCTCs displays a decent j_k of 17.24 mA cm^{-2} for ORR, which is 1.22 times larger than Pt/C (14.08 mA cm^{-2}) as shown in Fig. S26. The highest j_k in acid condition of Fe-SAs@NCTCs demonstrated the excellent intrinsic ORR activity of the designed active sites. The excellent acidic ORR activity of Fe-SAs@NCTCs is also supported by the fast reaction kinetic with a smallest Tafel plot slope of 54 mV dec^{-1} among the reference samples (Fig. 4h). Moreover, Fe-SAs@NCTCs catalyzing a four-electron ORR process in acidic condition is identified by the K-L plots as shown in Fig. 4i. The chronoamperometry test demonstrated the high stability of Fe-SAs@NCTCs for 40,000 s (Fig. S27). These results illustrate that the Fe-SAs@NCTCs achieved remarkable ORR performance in acidic solution, which is comparable to the Pt/C benchmark.

The electrocatalytic activity towards OER of Fe-SAs@NCTCs, Fe-SAs@CTCs, NCTCs and RuO_2 benchmark were assessed in 1.0 M KOH solution. The OER polarization curves (Fig. S28a) show that Fe-SAs@NCTCs have a significantly enhanced OER activity with a low potential of 1.63 V to reach a current density of 10 mA cm^{-2} ($E_{10} = 1.63$ V), which is comparable to that of the benchmark RuO_2 ($E_{10} = 1.57$ V). The Tafel plot slope (Fig. S28b) of Fe-SAs@NCTCs is 66 mV dec^{-1} , which is similar to RuO_2 (64 mV dec^{-1}), elucidating the fast OER

kinetics of Fe-SAs@NCTCs. To further clarify the OER reaction mechanism, RRDE test was conducted. As displayed in Fig. S28c, the collected ring current on RRDE is negligible even at the high applied potential range, evidencing that the OER on Fe-SAs@NCTCs would barely proceed via the two-electron pathways towards forming H_2O_2 . The OER Faradaic efficiency was then determined by the RRDE technique via estimating the contribution of the observed oxidation current [66]. As shown in Fig. S28d, when the OER current on disk electrode was set as a constant value of $300 \mu\text{A}$, the ring current could reach $110 \mu\text{A}$, showing a high faradaic efficiency of 95.5% and suggesting the oxidation current on Fe-SAs@NCTCs was entirely attributed to the OER. These results evidence that four-electron pathway with the formation of O_2 occurs on Fe-SAs@NCTCs during water oxidation. The ADT and chronoamperometry test were further conducted and revealed the excellent durability of Fe-SAs@NCTCs with negligible catalytic performance decrease (Fig. S29). Therefore, Fe-SAs@NCTCs is illustrated to be an efficient bifunctional ORR/OER electrocatalyst.

3.4. Zn-air battery performance

To assess the electrocatalytic performance in the real electrochemical energy conversion device, Zn-air batteries were assembled using Fe-SAs@NCTCs as the electrocatalysts in air cathode (Fig. 5a). A rechargeable Zn-air battery was assembled for comparison using a mixture of Pt/C and RuO_2 as the benchmark air cathode. Fig. 5b displays the galvanostatic discharge curve at the current density of 20 mA cm^{-2} . Fe-SAs@NCTCs possesses a stable discharge potential of 1.27 V, higher than that for Pt/C + RuO_2 based battery (1.20 V). Moreover, the discharge specific capacity of Fe-SAs@NCTCs-based battery reached 817 mAh g^{-1} , outperforming the Pt/C + RuO_2 based battery (782 mAh g^{-1}). As shown by the discharge curves in Fig. 5c, Fe-SAs@NCTCs-based battery exhibits higher discharge potentials than Pt/C + RuO_2 -based battery at the same discharge current. Moreover, power density curves reveal that Fe-SAs@NCTCs-based battery reached a peak power density of 171 mW cm^{-2} at the discharging current density of 254 mA cm^{-2} , which exceeds that of Pt/C + RuO_2 based Zn-air battery (155.2 mW cm^{-2} at 223 mA cm^{-2}). The discharge/charge performance was then gained by galvanostatic cycling the Zn-air batteries at a current density of 5 mA cm^{-2} as shown in Fig. 5d. When the battery continued running for 650 h, the discharge/charge voltage of Fe-SAs@NCTCs-based battery is retained. The discharge/charge voltage gap during the cycling test was further presented in Figs. 5e and 5f. As shown, the discharge/charge voltage gap is 0.75 V and the discharge voltage retained at 1.25 V after discharging/charging for 300 h, which corresponding to the round-trip efficiency of 62.5 %. Meanwhile, the discharge/charge voltage gap experienced a slight increase to 0.76 V with a round trip efficiency of 62 % after 600 h discharging/charging. In comparison, the battery assembled using Pt/C + RuO_2 electrocatalysts experienced a strike increase in the discharge/charge voltage gap to 0.85 V after testing for 120 h (Fig. S30). The performance of the assembled Zn-air batteries outperforms most of recently reported results (Table S11). The encouraging electrocatalytic activity and stability of Fe-SAs@NCTCs as air cathode in rechargeable Zn-air battery demonstrates its highly promising application under practical conditions.

4. Conclusion

In summary, inspired by theoretical calculations, which reveal the superiority of $\text{Fe}(\text{N}-\text{C}_2)_4$ -2N with nitrogen dopants in carbon skeletons to $\text{Fe}(\text{N}-\text{C}_2)_4$ active sites for catalyzing ORR, we designed Fe-N₄ single-atom electrocatalyst anchored in the hierarchically porous N-rich carbon support with tubular channels (denoted as Fe-SAs@NCTCs). The as-obtained Fe-SAs@NCTCs exhibits excellent ORR performances with high $E_{1/2}$ of 0.91 V (vs. RHE) in 0.1 M KOH and $E_{1/2}$ of 0.80 V (vs. RHE) in 0.1 M HClO_4 . Furthermore, when used the electrocatalysts in air cathode of Zn-air battery, it achieves high power density and excellent

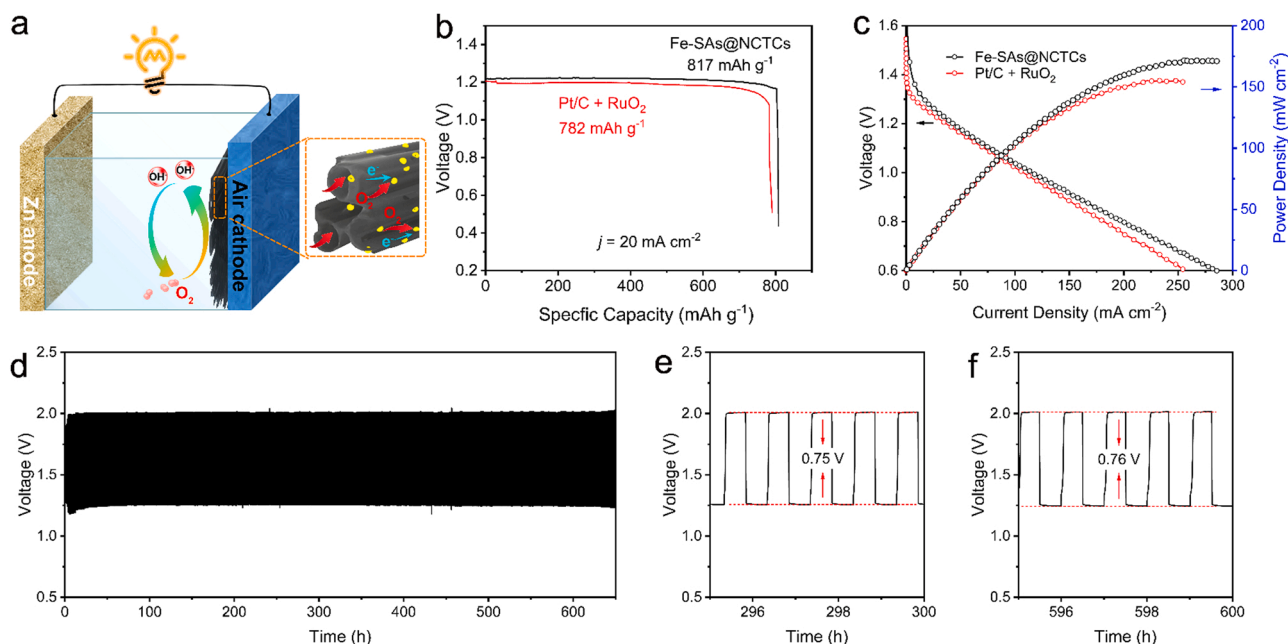


Fig. 5. (a) Schematic illustration of a self-assembled Zn–air battery. (b) Galvanostatic discharge profiles at 20 mA cm^{-2} . (c) Power density and discharge curves of Zn–air battery assembled using Fe-SAs@NCTCs or Pt/C + RuO_2 electrocatalysts. (d) Discharge/charge cycling curves of Zn–air battery assembled using Fe-SAs@NCTCs electrocatalysts at the current density of 5 mA cm^{-2} (1 h for each cycle). (e, f) Discharge/charge voltage gap of Zn–air batteries based on Fe-SAs@NCTCs during the cycling test.

discharge/charge stability, outperforming Pt/C + RuO_2 -based one. Therefore, the outstanding ORR activities of Fe-SAs@NCTCs can be attributed to the regulated electronic structure of active sites, plentiful accessible Fe-N₄ sites and fast mass transport. The strategy exemplified a promising way to designing hieratical porous architecture and altering the configuration of TM-N_x to build high-performance electrocatalysts.

CRediT authorship contribution statement

Fenghong Lu: Investigation, Visualization, Data curation. **Kaikai Fan:** Conceptualization, Investigation, Data curation, Formal analysis, Writing – original draft. **Lixiu Cui:** Investigation, Data curation. **Bin Li:** Visualization. **Yu Yang:** Visualization. **Lingbo Zong:** Conceptualization, Investigation, Visualization, Formal analysis, Writing – review & editing. **Lei Wang:** Supervision, Funding acquisition.

Declaration of Competing Interest

The authors declare that they have no known competing financial interests or personal relationships that could have appeared to influence the work reported in this paper.

Acknowledgements

F. L. and K. F. contributed equally to this work. This work was financially supported by the National Natural Science Foundation of China, China (Grant No. 52072197, 52172208, 21971132, 51702180), Natural Science Foundation of Shandong Province, China (ZR2019MB042), Major Scientific and Technological Innovation Project of Shandong Province, China (2019JZZY020405), and Major Basic Research Program of Natural Science Foundation of Shandong Province under Grant, China (ZR2020ZD09). This research was undertaken on the X-ray absorption spectroscopy (XAS) beamlines at Beijing Synchrotron Radiation Facility (1W1B).

Appendix A. Supporting information

Supplementary data associated with this article can be found in the online version at [doi:10.1016/j.apcatb.2022.121464](https://doi.org/10.1016/j.apcatb.2022.121464).

References

- [1] L. Jiao, J. Li, L.L. Richard, Q. Sun, T. Stracensky, E. Liu, M.T. Sougrati, Z. Zhao, F. Yang, S. Zhong, H. Xu, S. Mukerjee, Y. Huang, D.A. Cullen, J.H. Park, M. Ferrandon, D.J. Myers, F. Jaouen, Q. Jia, Chemical vapour deposition of Fe-N-C oxygen reduction catalysts with full utilization of dense Fe-N₄ sites, *Nat. Mater.* 20 (2021) 1385–1391, <https://doi.org/10.1038/s41563-021-01030-2>.
- [2] X. Wan, X. Liu, Y. Li, R. Yu, L. Zheng, W. Yan, H. Wang, M. Xu, J. Shui, Fe-N-C electrocatalyst with dense active sites and efficient mass transport for high-performance proton exchange membrane fuel cells, *Nat. Catal.* 2 (2019) 259–268, <https://doi.org/10.1038/s41929-019-0237-3>.
- [3] X. Fu, G. Jiang, G. Wen, R. Gao, S. Li, M. Li, J. Zhu, Y. Zheng, Z. Li, Y. Hu, L. Yang, Z. Bai, A. Yu, Z. Chen, Densely accessible Fe-N_x active sites decorated mesoporous carbon-spheres for oxygen reduction towards high performance aluminum-air flow batteries, *Appl. Catal. B: Environ.* 293 (2021) 120176–120184, <https://doi.org/10.1016/j.apcatb.2021.120176>.
- [4] Y. Cheng, J. Zhang, X. Wu, C. Tang, S. Yang, P. Su, L. Thomsen, F. Zhao, S. Lu, J. Liu, S.P. Jiang, A template-free method to synthesize high density iron single atoms anchored on carbon nanotubes for high temperature polymer electrolyte membrane fuel cells, *Nano Energy* 80 (2021) 105534–105542, <https://doi.org/10.1016/j.nanoen.2020.105534>.
- [5] M. Lefevre, E. Proietti, F. Jaouen, J.P. Dodelet, Iron-based catalysts with improved oxygen reduction activity in polymer electrolyte fuel cells, *Science* 324 (2009) 71–74, <https://doi.org/10.1126/science.1170051>.
- [6] L. Cui, K. Fan, L. Zong, F. Lu, M. Zhou, B. Li, L. Zhang, L. Feng, X. Li, Y. Chen, L. Wang, Sol-gel pore-sealing strategy imparts tailored electronic structure to the atomically dispersed Ru sites for efficient oxygen reduction reaction, *Energy Storage Mater.* 44 (2022) 469–476, <https://doi.org/10.1016/j.ensm.2021.11.007>.
- [7] C. Gu, J. Li, J.P. Liu, H. Wang, Y. Peng, C.S. Liu, Conferring supramolecular guanosine gel nanofiber with ZIF-67 for high-performance oxygen reduction catalysis in rechargeable zinc-air batteries, *Appl. Catal. B: Environ.* 286 (2021) 119888–119897, [doi: 10.1016/j.apcatb.2021.119888](https://doi.org/10.1016/j.apcatb.2021.119888).
- [8] L. Zong, W. Wu, S. Liu, H. Yin, Y. Chen, C. Liu, K. Fan, X. Zhao, X. Chen, F. Wang, Y. Yang, L. Wang, S. Feng, Metal-free, active nitrogen-enriched, efficient bifunctional oxygen electrocatalyst for ultrastable zinc-air batteries, *Energy Storage Mater.* 27 (2020) 514–521, <https://doi.org/10.1016/j.ensm.2019.12.013>.
- [9] Y. Wang, Z. Li, P. Zhang, Y. Pan, Y. Zhang, Q. Cai, S.R.P. Silva, J. Liu, G. Zhang, X. Sun, Z. Yan, Flexible carbon nanofiber film with diatomic Fe-Co sites for efficient oxygen reduction and evolution reactions in wearable zinc-air batteries, *Nano Energy* 87 (2021) 106147–106158, <https://doi.org/10.1016/j.nanoen.2021.106147>.

- [10] P. Su, W. Huang, J. Zhang, U. Guharoy, Q. Du, Q. Sun, Q. Jiang, Y. Cheng, J. Yang, X. Zhang, Y. Liu, S.P. Jiang, J. Liu, Fe atoms anchored on defective nitrogen doped hollow carbon spheres as efficient electrocatalysts for oxygen reduction reaction, *Nano Res.* 14 (2020) 1069–1077, <https://doi.org/10.1007/s12274-020-3151-8>.
- [11] M. Xiao, L. Gao, Y. Wang, X. Wang, J. Zhu, Z. Jin, C. Liu, H. Chen, G. Li, J. Ge, Q. He, Z. Wu, Z. Chen, W. Xing, Engineering energy level of metal center: Ru single-atom site for efficient and durable oxygen reduction catalysis, *J. Am. Chem. Soc.* 141 (2019) 19800–19806, <https://doi.org/10.1021/jacs.9b09234>.
- [12] L. Deng, L. Qiu, R. Hu, L. Yao, Z. Zheng, X. Ren, Y. Li, C. He, Restricted diffusion preparation of fully-exposed Fe single-atom catalyst on carbon nanospheres for efficient oxygen reduction reaction, *Appl. Catal. B: Environ.* 305 (2022) 121058–121067, <https://doi.org/10.1016/j.apcatb.2021.121058>.
- [13] X. Qu, Y. Han, Y. Chen, J. Lin, G. Li, J. Yang, Y. Jiang, S. Sun, Stepwise pyrolysis treatment as an efficient strategy to enhance the stability performance of Fe-N_x/C electrocatalyst towards oxygen reduction reaction and proton exchange membrane fuel cell, *Appl. Catal. B: Environ.* 295 (2021) 120311–120321, <https://doi.org/10.1016/j.apcatb.2021.120311>.
- [14] Y. Zhou, G. Chen, Q. Wang, D. Wang, X. Tao, T. Zhang, X. Feng, K. Müllen, Fe-N-C electrocatalysts with densely accessible Fe-N₄ sites for efficient oxygen reduction reaction, *Adv. Funct. Mater.* (2021) 2102420–2102428, <https://doi.org/10.1002/adfm.202102420>.
- [15] H. Sun, M. Wang, S. Zhang, S. Liu, X. Shen, T. Qian, X. Niu, J. Xiong, C. Yan, Boosting oxygen dissociation over bimetal sites to facilitate oxygen reduction activity of zinc-air battery, *Adv. Funct. Mater.* 31 (2020) 2006533–2006540, <https://doi.org/10.1002/adfm.202006533>.
- [16] X. Zhong, S. Ye, J. Tang, Y. Zhu, D. Wu, M. Gu, H. Pan, B. Xu, Engineering Pt and Fe dual-metal single atoms anchored on nitrogen-doped carbon with high activity and durability towards oxygen reduction reaction for zinc-air battery, *Appl. Catal. B: Environ.* 286 (2021) 119891–119898, <https://doi.org/10.1016/j.apcatb.2021.119891>.
- [17] M. Wang, W. Yang, X. Li, Y. Xu, L. Zheng, C. Su, B. Liu, Atomically dispersed Fe-heteroatom (N, S) bridge sites anchored on carbon nanosheets for promoting oxygen reduction reaction, *ACS Energy Lett.* 6 (2021) 379–386, <https://doi.org/10.1021/acseenergylett.0c02484>.
- [18] Q. Li, W. Chen, H. Xiao, Y. Gong, Z. Li, L. Zheng, X. Zheng, W. Yan, W.C. Cheong, R. Shen, N. Fu, L. Gu, Z. Zhuang, C. Chen, D. Wang, Q. Peng, J. Li, Y. Li, Fe isolated single atoms on S, N codoped carbon by copolymer pyrolysis strategy for highly efficient oxygen reduction reaction, *Adv. Mater.* 30 (2018) 1800588–1800593, <https://doi.org/10.1002/adma.201800588>.
- [19] Y. Mun, S. Lee, K. Kim, S. Kim, S. Lee, J.W. Han, J. Lee, Versatile strategy for tuning ORR activity of a single Fe-N₄ site by controlling electron-withdrawing/donating properties of a carbon plane, *J. Am. Chem. Soc.* 141 (2019) 6254–6262, <https://doi.org/10.1021/jacs.8b13543>.
- [20] K. Yuan, D. Lutzenkirchen-Hecht, L. Li, L. Shuai, Y. Li, R. Cao, M. Qiu, X. Zhuang, M.K.H. Leung, Y. Chen, U. Scherf, Boosting oxygen reduction of single iron active sites via geometric and electronic engineering: nitrogen and phosphorus dual coordination, *J. Am. Chem. Soc.* 142 (2020) 2404–2412, <https://doi.org/10.1021/jacs.9b11852>.
- [21] L. Yu, Y. Li, Y. Ruan, Dynamic control of sacrificial bond transformation in the Fe-N-C single-atom catalyst for molecular oxygen reduction, *Angew. Chem. Int. Ed.* 60 (2021) 25296–25301, <https://doi.org/10.1002/anie.202111761>.
- [22] Z. Chen, H. Niu, J. Ding, H. Liu, P.H. Chen, Y.H. Lu, Y.R. Lu, W. Zuo, L. Han, Y. Guo, S.F. Hung, Y. Zhai, Unraveling the origin of sulfur-doped Fe-N-C single atom catalyst for enhanced oxygen reduction activity: effect of Fe-spin state tuning, *Angew. Chem. Int. Ed.* (2021) 25404–25410, <https://doi.org/10.1002/anie.202110243>.
- [23] N. Zhang, T. Zhou, M. Chen, H. Feng, R. Yuan, Ca Zhong, W. Yan, Y. Tian, X. Wu, W. Chu, C. Wu, Y. Xie, High-purity pyrrole-type FeN₄ sites as a superior oxygen reduction electrocatalyst, *Energy Environ. Sci.* 13 (2020) 111–118, <https://doi.org/10.1039/C9EE03027A>.
- [24] M. Mazzucato, G. Daniel, A. Mehmood, T. Kosmala, G. Granozzi, A. Kucernak, C. Durante, Effects of the induced micro- and meso-porosity on the single site density and turn over frequency of Fe-N-C carbon electrodes for the oxygen reduction reaction, *Appl. Catal. B: Environ.* 291 (2021) 120068–120081, <https://doi.org/10.1016/j.apcatb.2021.120068>.
- [25] S.H. Lee, J. Kim, D.Y. Chung, J.M. Yoo, H.S. Lee, M.J. Kim, B.S. Mun, S.G. Kwon, Y. E. Sung, T. Hyeon, Design principle of Fe-N-C electrocatalysts: how to optimize multimodal porous structures? *J. Am. Chem. Soc.* 141 (2019) 2035–2045, <https://doi.org/10.1021/jacs.8b11129>.
- [26] M. Qiao, Y. Wang, Q. Wang, G. Hu, X. Mamat, S. Zhang, S. Wang, Hierarchically ordered porous carbon with atomically dispersed FeN₄ for ultraefficient oxygen reduction reaction in proton-exchange membrane fuel cells, *Angew. Chem. Int. Ed.* 59 (2020) 2688–2694, <https://doi.org/10.1002/anie.201914123>.
- [27] S. Zhang, W. Yang, Y. Liang, X. Yang, M. Cao, R. Cao, Template-free synthesis of non-noble metal single-atom electrocatalyst with N-doped holey carbon matrix for highly efficient oxygen reduction reaction in zinc-air batteries, *Appl. Catal. B: Environ.* 285 (2021) 119780–119786, <https://doi.org/10.1016/j.apcatb.2020.119780>.
- [28] Z. Liu, Y. Du, P. Zhang, Z. Zhuang, D. Wang, Bringing catalytic order out of chaos with nitrogen-doped ordered mesoporous carbon, *Mater.* 4 (2021) 3161–3194, <https://doi.org/10.1016/j.matt.2021.07.019>.
- [29] L. Zong, K. Fan, W. Wu, L. Cui, L. Zhang, B. Johannessen, D. Qi, H. Yin, Y. Wang, P. Liu, L. Wang, H. Zhao, Anchoring single copper atoms to microporous carbon spheres as high-performance electrocatalyst for oxygen reduction reaction, *Adv. Funct. Mater.* 31 (2021) 2104864–2104874, <https://doi.org/10.1002/adfm.202104864>.
- [30] J. Li, H. Zhang, W. Samarakoon, W. Shan, D.A. Cullen, S. Karakalos, M. Chen, D. Gu, K.L. More, G. Wang, Z. Feng, Z. Wang, G. Wu, Thermally driven structure and performance evolution of atomically dispersed FeN₄ sites for oxygen reduction, *Angew. Chem. Int. Ed.* 58 (2019) 18971–18980, <https://doi.org/10.1002/anie.201909312>.
- [31] X. Xie, L. Peng, H. Yang, G.I.N. Waterhouse, L. Shang, T. Zhang, MIL-101-derived mesoporous carbon supporting highly exposed Fe single-atom sites as efficient oxygen reduction reaction catalysts, *Adv. Mater.* 33 (2021) 2101038–2101045, <https://doi.org/10.1002/adma.202101038>.
- [32] X. Zhang, S. Zhang, Y. Yang, L. Wang, Z. Mu, H. Zhu, X. Zhu, H. Xing, H. Xia, B. Huang, J. Li, S. Guo, E. Wang, A general method for transition metal single atoms anchored on honeycomb-like nitrogen-doped carbon nanosheets, *Adv. Mater.* 32 (2020) 1906905–1906912, <https://doi.org/10.1002/adma.201906905>.
- [33] C. Zhu, Q. Shi, B.Z. Xu, S. Fu, G. Wan, C. Yang, S. Yao, J. Song, H. Zhou, D. Du, S. P. Beckman, D. Su, Y. Lin, Hierarchically porous M-N-C (M = Co and Fe) single-atom electrocatalysts with robust MN_x active moieties enable enhanced ORR performance, *Adv. Energy Mater.* 8 (2018) 1801956–1801963, <https://doi.org/10.1002/aenm.201801956>.
- [34] G. Kresse, J. Furthmüller, Efficiency of ab-initio total energy calculations for metals and semiconductors using a plane-wave basis set, *Comput. Mater. Sci.* 6 (1996) 15–50, [https://doi.org/10.1016/0927-0256\(96\)00008-0](https://doi.org/10.1016/0927-0256(96)00008-0).
- [35] S. Ehrlich, J. Moellmann, W. Reckien, T. Bredow, S. Grimme, System-dependent dispersion coefficients for the DFT-D3 treatment of adsorption processes on ionic surfaces, *Chemphyschem* 12 (2011) 3414–3420, <https://doi.org/10.1002/cphc.201100521>.
- [36] G. Zhu, F. Liu, Y. Wang, Z. Wei, W. Wang, Systematic exploration of N,C coordination effects on the ORR performance of Mn-N_x doped graphene catalysts based on DFT calculations, *Phys. Chem. Chem. Phys.* 21 (2019) 12826–12836, <https://doi.org/10.1039/c9cp02155h>.
- [37] J. Zhao, S. Ji, C. Guo, H. Li, J. Dong, P. Guo, D. Wang, Y. Li, F.D. Toste, A heterogeneous iridium single-atom-site catalyst for highly regioselective carbenoid O–H bond insertion, *Nat. Catal.* 4 (2021) 523–531, <https://doi.org/10.1038/s41929-021-00637-7>.
- [38] M. Xiao, Y. Chen, J. Zhu, H. Zhang, X. Zhao, L. Gao, X. Wang, J. Zhao, J. Ge, Z. Jiang, S. Chen, C. Liu, W. Xing, Climbing the apex of the ORR volcano plot via binuclear site construction: electronic and geometric engineering, *J. Am. Chem. Soc.* 141 (2019) 17763–17770, <https://doi.org/10.1021/jacs.9b08362>.
- [39] L. Hu, C. Dai, L. Chen, Y. Zhu, Y. Hao, Q. Zhang, L. Gu, X. Feng, S. Yuan, L. Wang, B. Wang, Metal-triazolate-framework derived FeN₄(Cl)(1) single-atom catalysts with hierarchical porosity for the oxygen reduction reaction, *Angew. Chem. Int. Ed.* (2021) 27324–27329, <https://doi.org/10.1002/anie.202113895>.
- [40] M. Xiao, Z. Xing, Z. Jin, C. Liu, J. Ge, J. Zhu, Y. Wang, X. Zhao, Z. Chen, Preferentially engineering FeN₄ edge sites onto graphitic nanosheets for highly active and durable oxygen electrocatalysis in rechargeable Zn-air batteries, *Adv. Mater.* 32 (2020) 2004900–2004908, <https://doi.org/10.1002/adma.202004900>.
- [41] J. Zhang, H. Yang, B. Liu, Coordination engineering of single-atom catalysts for the oxygen reduction reaction: a review, *Adv. Energy Mater.* 11 (2020) 2002473–2002492, <https://doi.org/10.1002/aenm.202002473>.
- [42] F. Calle-Vallejo, J.I. Martínez, J. Rossmeisl, Density functional studies of functionalized graphitic materials with late transition metals for Oxygen Reduction Reactions, *Phys. Chem. Chem. Phys.* 13 (2011) 15639–15643, <https://doi.org/10.1039/c1cp21228a>.
- [43] J.S. Shen, Q.G. Cai, Y.B. Jiang, H.W. Zhang, Anion-triggered melamine based self-assembly and hydrogel, *Chem. Commun.* 46 (2010) 6786–6788, <https://doi.org/10.1039/c0cc02030c>.
- [44] R. Mi, C. Chen, T. Keplinger, Y. Pei, S. He, D. Liu, J. Li, J. Dai, E. Hitz, B. Yang, I. Burgert, L. Hu, Scalable aesthetic transparent wood for energy efficient buildings, *Nat. Commun.* 11 (2020) 3836–3845, <https://doi.org/10.1038/s41467-020-17513-w>.
- [45] P. Mu, Z. Zhang, W. Bai, J. He, H. Sun, Z. Zhu, W. Liang, A. Li, Superwetting monolithic hollow-carbon-nanotubes aerogels with hierarchically nanoporous structure for efficient solar steam generation, *Adv. Energy Mater.* 9 (2019) 1802158–1802166, <https://doi.org/10.1002/aenm.201802158>.
- [46] X. Han, X. Ling, D. Yu, D. Xie, L. Li, S. Peng, C. Zhong, N. Zhao, Y. Deng, W. Hu, Atomically dispersed binary Co-Ni sites in nitrogen-doped hollow carbon nanocubes for reversible oxygen reduction and evolution, *Adv. Mater.* 31 (2019) 1905622–1905630, <https://doi.org/10.1002/adma.201905622>.
- [47] D. Xia, X. Yang, L. Xie, Y. Wei, W. Jiang, M. Dou, X. Li, J. Li, L. Gan, F. Kang, Direct growth of carbon nanotubes doped with single atomic Fe-N₄ active sites and neighboring graphitic nitrogen for efficient and stable oxygen reduction electrocatalysis, *Adv. Funct. Mater.* 29 (2019) 1906174–1906183, <https://doi.org/10.1002/adfm.201906174>.
- [48] Y. Chen, J. Wei, M.S. Duyar, V.V. Ordonsky, A.Y. Khodakov, J. Liu, Carbon-based catalysts for fischer-tropsch synthesis, *Chem. Soc. Rev.* 50 (2021) 2337–2366, <https://doi.org/10.1039/D0CS00905A>.
- [49] F. Jiang, T. Li, Y. Li, Y. Zhang, A. Gong, J. Dai, E. Hitz, W. Luo, L. Hu, Wood-based nanotechnologies toward sustainability, *Adv. Mater.* 30 (2018) 1703453–1703491, <https://doi.org/10.1002/adma.201703453>.
- [50] X. Peng, L. Zhang, Z. Chen, L. Zhong, D. Zhao, X. Chi, X. Zhao, L. Li, X. Lu, K. Leng, C. Liu, W. Liu, W. Tang, K.P. Loh, Hierarchically porous carbon plates derived from wood as bifunctional ORR/OER electrodes, *Adv. Mater.* 31 (2019) 1900341–1900347, <https://doi.org/10.1002/adma.201900341>.
- [51] M. Thommes, K. Kaneko, A.V. Neimark, J.P. Olivier, F. Rodriguez-Reinoso, J. Rouquerol, K.S.W. Sing, Physisorption of gases, with special reference to the evaluation of surface area and pore size distribution (IUPAC Technical Report), *Pure Appl. Chem.* 87 (2015) 1051–1069, <https://doi.org/10.1515/pac-2014-1117>.

- [52] H. Shen, E. Gracia-Espino, J. Ma, K. Zang, J. Luo, L. Wang, S. Gao, X. Mamat, G. Hu, T. Wagberg, S. Guo, Synergistic effects between atomically dispersed Fe-N-C and C-S-C for the oxygen reduction reaction in acidic media, *Angew. Chem. Int. Ed.* 56 (2017) 13800–13804, <https://doi.org/10.1002/anie.201706602>.
- [53] X. Chen, D.-D. Ma, B. Chen, K. Zhang, R. Zou, X.-T. Wu, Q.-L. Zhu, Metal-organic framework-derived mesoporous carbon nanoframes embedded with atomically dispersed Fe-N active sites for efficient bifunctional oxygen and carbon dioxide electroreduction, *Appl. Catal. B: Environ.* 267 (2020) 118720–118729, <https://doi.org/10.1016/j.apcatb.2020.118720>.
- [54] S.-G. Han, D.-D. Ma, S.-H. Zhou, K. Zhang, W.-B. Wei, Y. Du, X.-T. Wu, Q. Xu, R. Zou, Q.-L. Zhu, Fluorine-tuned single-atom catalysts with dense surface Ni-N₄ sites on ultrathin carbon nanosheets for efficient CO₂ electroreduction, *Appl. Catal. B: Environ.* 283 (2021) 119591–119599, <https://doi.org/10.1016/j.apcatb.2020.119591>.
- [55] Y. Chen, Z. Li, Y. Zhu, D. Sun, X. Liu, L. Xu, Y. Tang, Atomic Fe dispersed on N-doped carbon hollow nanospheres for high-efficiency electrocatalytic oxygen reduction, *Adv. Mater.* 31 (2019) 1806312–1806319, <https://doi.org/10.1002/adma.201806312>.
- [56] F. Pan, B. Li, E. Sarnello, Y. Fei, X. Feng, Y. Gang, X. Xiang, L. Fang, T. Li, Y.H. Hu, G. Wang, Y. Li, Pore-edge tailoring of single-atom iron-nitrogen sites on graphene for enhanced CO₂ reduction, *ACS Catal.* 10 (2020) 10803–10811, <https://doi.org/10.1021/acscatal.0c02499>.
- [57] L. Jing, Q. Tian, P. Su, H. Li, Y. Zheng, C. Tang, J. Liu, Mesoporous Co-O-C nanosheets for electrochemical production of hydrogen peroxide in acidic medium, *J. Mater. Chem. A* 10 (2022) 4068–4075, <https://doi.org/10.1039/D1TA10416K>.
- [58] X. Wang, S. Qiu, J. Feng, Y. Tong, F. Zhou, Q. Li, L. Song, S. Chen, K.H. Wu, P. Su, S. Ye, F. Hou, S.X. Dou, H.K. Liu, G.Q. Max Lu, C. Sun, J. Liu, J. Liang, Confined Fe-Cu clusters as sub-nanometer reactors for efficiently regulating the electrochemical nitrogen reduction reaction, *Adv. Mater.* 32 (2020) 2004382–2004391, <https://doi.org/10.1002/adma.202004382>.
- [59] Z. Chen, A. Huang, K. Yu, T. Cui, Z. Zhuang, S. Liu, J. Li, R. Tu, K. Sun, X. Tan, J. Zhang, D. Liu, Y. Zhang, P. Jiang, Y. Pan, C. Chen, Q. Peng, Y. Li, Fe₁N₄-O₁ site with axial Fe-O coordination for highly selective CO₂ reduction over a wide potential range, *Energy Environ. Sci.* 14 (2021) 3430–3437, <https://doi.org/10.1039/D1EE00569C>.
- [60] M. Wilke, F. Farges, P.-E. Petit, G.E. Brown, F. Martin, Oxidation state and coordination of Fe in minerals: An Fe K-XANES spectroscopic study, *Am. Miner.* 86 (2001) 714–730, <https://doi.org/10.2138/am-2001-5-612>.
- [61] A.J. Berry, H.S.C. O'Neill, K.D. Jayasuriya, S.J. Campbell, G.J. Foran, XANES calibrations for the oxidation state of iron in a silicate glass, *Am. Min.* 88 (2003) 967–977, <https://doi.org/10.2138/am-2003-0704>.
- [62] X. Ao, W. Zhang, B. Zhao, Y. Ding, G. Nam, L. Soule, A. Abdelhafiz, C. Wang, M. Liu, Atomically dispersed Fe-N-C decorated with Pt-alloy core-shell nanoparticles for improved activity and durability towards oxygen reduction, *Energy Environ. Sci.* 13 (2020) 3032–3040, <https://doi.org/10.1039/D0EE00832J>.
- [63] Y. Chen, S. Ji, S. Zhao, W. Chen, J. Dong, W.C. Cheong, R. Shen, X. Wen, L. Zheng, A.I. Rykov, S. Cai, H. Tang, Z. Zhuang, C. Chen, Q. Peng, D. Wang, Y. Li, Enhanced oxygen reduction with single-atomic-site iron catalysts for a zinc-air battery and hydrogen-air fuel cell, *Nat. Commun.* 9 (2018) 5422–5433, <https://doi.org/10.1038/s41467-018-07850-2>.
- [64] H. Xu, H. Jia, H. Li, J. Liu, X. Gao, J. Zhang, M. Liu, D. Sun, S. Chou, F. Fang, R. Wu, Dual carbon-hosted Co-N₃ enabling unusual reaction pathway for efficient oxygen reduction reaction, *Appl. Catal. B: Environ.* 297 (2021) 120390–120398, <https://doi.org/10.1016/j.apcatb.2021.120390>.
- [65] Q. Wang, Y. Yang, F. Sun, G. Chen, J. Wang, L. Peng, W.T. Chen, L. Shang, J. Zhao, D. Sun-Waterhouse, T. Zhang, G.I.N. Waterhouse, Molten NaCl-assisted synthesis of porous Fe-N-C electrocatalysts with a high density of catalytically accessible FeN₄ active sites and outstanding oxygen reduction reaction performance, *Adv. Energy Mater.* 11 (2021) 2100219–2100227, <https://doi.org/10.1002/aenm.202100219>.
- [66] S. Zhao, Y. Wang, J. Dong, C.-T. He, H. Yin, P. An, K. Zhao, X. Zhang, C. Gao, L. Zhang, J. Lv, J. Wang, J. Zhang, A.M. Khattak, N.A. Khan, Z. Wei, J. Zhang, S. Liu, H. Zhao, Z. Tang, Ultrathin metal-organic framework nanosheets for electrocatalytic oxygen evolution, *Nat. Energy* 1 (2016) 16184–16193, <https://doi.org/10.1038/nenergy.2016.184>.